



**HAL**  
open science

# Microstructure evolution in nano-reinforced ferritic steel processed by mechanical alloying and spark plasma sintering

Xavier Boulnat, Michel Perez, Damien Fabregue, Thierry Douillard,  
Marie-Hélène Mathon, Yann de Carlan

## ► To cite this version:

Xavier Boulnat, Michel Perez, Damien Fabregue, Thierry Douillard, Marie-Hélène Mathon, et al.. Microstructure evolution in nano-reinforced ferritic steel processed by mechanical alloying and spark plasma sintering. Metallurgical and Materials Transactions A, 2014, 45 (3), pp.1485-1497. 10.1007/s11661-013-2107-y . hal-01540098

**HAL Id: hal-01540098**

**<https://hal.science/hal-01540098>**

Submitted on 24 Nov 2023

**HAL** is a multi-disciplinary open access archive for the deposit and dissemination of scientific research documents, whether they are published or not. The documents may come from teaching and research institutions in France or abroad, or from public or private research centers.

L'archive ouverte pluridisciplinaire **HAL**, est destinée au dépôt et à la diffusion de documents scientifiques de niveau recherche, publiés ou non, émanant des établissements d'enseignement et de recherche français ou étrangers, des laboratoires publics ou privés.

# Microstructure Evolution in Nano-reinforced Ferritic Steel Processed By Mechanical Alloying and Spark Plasma Sintering

Xavier Boulnat, Michel Perez, Damien Fabregue,  
Thierry Douillard, Marie-hélène Mathon, and Yann de Carlan

Oxide-dispersion strengthened ferritic steel was produced by high-energy attrition, leading to a complex nanostructure with deformed ferritic grains. After mechanical alloying, the powder was then consolidated by spark plasma sintering (SPS) using various thermo-mechanical treatments. Hot isostatic pressing (HIP) was also performed on the same powder for comparison. Above 1123 K (850 °C), SPS consolidation-induced heterogeneous microstructure composed of ultra-fine-grained regions surrounded by larger grains. Spatial distribution of the stored energy was measured in the bimodal microstructure using the Kernel average misorientation. In contrary to large recrystallized grains, ultra-fine grains are still substructured with low-angle grain boundaries. The precipitation kinetics of the nano-oxides during consolidation was determined by small-angle neutron scattering. Precipitation mainly occurred during the heating stage, leading to a high density of nanoclusters that are of prime importance for the mechanical properties. Other coarser titanium-enriched oxides were also detected. The multiscale characterization allowed us to understand and model the evolution of the complex microstructure. An analytical evaluation of the contributing mechanisms explains the appearance of the complex grain structure and its thermal stability during further heat treatments. Inhomogeneous distribution of plastic deformation in the powder is the major cause of heterogeneous recrystallization and further grain growth during hot consolidation. Then, the thermal stability of coherent nano-oxides is responsible for effective grain boundary pinning in recovered regions where the driving pressure for recrystallization is lowered. This scenario is confirmed in both SPSed and HIPed materials.

## I. INTRODUCTION

HIGH-CHROMIUM ferritic oxide-dispersion strengthened (ODS) steels displayed considerable interest for high-temperature applications.<sup>[1-3]</sup> These materials exhibit excellent creep properties due to a specific microstructure reinforced by a very fine and homogeneous dispersion of nano-oxides. This requires the use of powder metallurgy where yttria particles and pre-alloyed ferritic powder are mixed together. Then, hot isostatic pressing (HIP) and/or hot extrusion (HE) are conventional processes to consolidate the materials.<sup>[4]</sup> Recently, spark plasma sintering (SPS) has emerged as a novel tool to process nanostructured materials.<sup>[5-8]</sup> This technique has been assessed for mechanically alloyed

ODS ferritic steels, providing dense materials with a fine and heterogeneous microstructure.<sup>[9]</sup> The appearance of bimodal grain structure composed of ultrafine grains with coarser grains has been referred to enhance ductility when comparing to monomodal nanostructured materials.<sup>[9-13]</sup> Srinivasarao *et al.*<sup>[14]</sup> tailored the nanosized to coarse grains ratio to obtain excellent compromise between tensile strength and elongation with a milled iron powder consolidated by SPS. Austenitic and martensitic steels also show heterogeneous microstructures after SPS consolidation, depending upon the use of dry or wet milling process.<sup>[15]</sup> Other metallic materials such as Fe-Mo,<sup>[16]</sup> Mg-Mn-Zr<sup>[17]</sup> showed similar properties.

As these materials are produced by powder metallurgy, the link between the initial nanostructure and the resulting microstructural features and mechanical properties of the final compacts needs to be better understood. More specifically, ODS steels involve second-phase particles that are known to drastically influence either the subgrain or the grain growth.<sup>[18-21]</sup> Heterogeneous grain structure is often reported in ODS steels but such structure is tough to tailor and make reproducible. One of the main reasons is that the whole precipitation state in ODS steels depends upon numerous factors among which the consolidation parameters and the content of yttrium and titanium. Many studies were focused on nanosized particles,<sup>[22,23]</sup> rarely with an

---

XAVIER BOULNAT, Ph.D. Student, and YANN DE CARLAN, Researcher, are with the Service de Recherches Métallurgiques Appliquées, CEA, DEN, 91191 Gif-sur-Yvette, France. Contact e-mail: xavier.boulnat@cea.fr MICHEL PEREZ, Professor, DAMIEN FABREGUE, Associate Professor, and THIERRY DOUILLARD, Researcher, are with the Université de Lyon, INSA-Lyon, MATEIS UMR CNRS 5510, 69621 Villeurbanne, France. MARIE-HÉLÈNE MATHON, Researcher, is with the Laboratoire Léon Brillouin, CEA-CNRS, CEA/Saclay, 91191 Gif-sur-Yvette, France.

overall view of the precipitation state in the alloy. This is why the influence of precipitation on grain growth has been scarcely studied. Therefore, one needs to understand both the role of the initial structure due to powder metallurgical processes and the coupling between grain growth and precipitation in industrial ODS alloys.

In this sense, this work aims to use multiscale characterization at each processing step for both SPS and HIP to describe how the grain structure and the precipitation state evolve and influence each other. Specially, SPS was used as a tool for obtaining different microstructures. The numerous microstructural features acquired in this study were used as an input to discuss the heterogeneous recrystallization and the further stability of such microstructure.

## II. EXPERIMENTAL

### A. Materials Processing

The base powder of high-Chromium ferritic steel was produced by gas atomization by Auvert and Duval. The powder particles were spherical with a mean diameter of 70  $\mu\text{m}$ . They were composed of iron matrix with chromium (14 wt pct), tungsten (1 wt pct), and other alloying elements such as titanium, manganese, and silicon. The ferritic powder was milled with yttria particles ( $D < 100$  nm) at Plansee SE, using an industrial high-energy attritor under hydrogen atmosphere. The two powders were directly fed into the stainless steel tank with no premixing and agitated by a vertical shaft rotating at high speed for 12 hours. This duration was found to be a good compromise between homogeneity and minimization of eventual contamination in carbon and aluminum. The milled powder was produced by batches of 10 to 13 kg. The composition of the milled powder measured by electron probe microanalysis is reported in Table I. The powder was then compacted by various thermo-mechanical treatments in the SPS device HP D 25 of FCT Systeme Company. SPS compacts were cylindrical pellets of 20 mm diameter and 6 mm height. An average sintering pressure of 76 MPa was applied. The latter was applied before heating at a rate of 500  $\text{K min}^{-1}$  up to the holding temperature, which was chosen at 1123 K, 1323 K, and 1423 K (850  $^{\circ}\text{C}$ , 1050  $^{\circ}\text{C}$ , and 1150  $^{\circ}\text{C}$ ). The dwelling time at maximum temperature was 5 minutes. Finally, cooling was induced by direct contact with water-cooled punches. Two compacts were made for each dwelling temperature. The optimized processing parameters for fully dense compacts of larger dimensions (60 mm diameter, 20 mm height) resulting in excellent mechanical properties are reported in Reference 9. In this study, remaining

porosity was observed on the samples consolidated at temperatures lower than 1423 K (1150  $^{\circ}\text{C}$ ). The temperature given in this work was measured by a vertical pyrometer and tailored by an optimized PID controller. In order to compare the microstructural behavior of novel SPSed ODS materials to more conventional ODS materials, HIP was performed on the same milled powder. Hot consolidation was performed at 1423 K (1150  $^{\circ}\text{C}$ ) for 3 hours with a heating rate of 5  $\text{K min}^{-1}$  under an average pressure of 100 MPa. HIP compacts were cylindrical parts of 60 mm diameter and 50 mm height.

### B. Characterization

For microstructure characterization, specimen having a cross-section with 10 mm  $\times$  10 mm and a thickness of 1 mm were machined from the center region of the compacts to avoid edge effects. Yet, microhardness and global SEM observations confirmed that there was no evidence of microstructural variation between the center region and the edge regions.

#### 1. Electron microscopy

Grains were characterized by a scanning electron microscope (SEM) Zeiss Supra 55 VP with field-emission gun (FEG) associated with an electron backscatter diffraction (EBSD) Oxford system for orientation and grain size measurement. Acquisition step size ranged from 10 to 60 nm with a tension of 15 kV. Cross-sectioning and imaging on milled powder particles were performed using a FIB/SEM workstation combining a SIINT zeta FIB column (Seiko Instruments) with a Gemini column. The NVision 40 platform was also equipped with a multiple SIINT gas injection system (GIS).

Grain size distributions were measured by EBSD and calculated with the post-processing software Channel 5. The size distribution was plotted in area fraction instead of number fraction, the latter not being pertinent for heterogeneous grain structure.<sup>[24,25]</sup> Therefore, the mean diameter  $D_{\text{mean}}^A$  was calculated as:

$$D_{\text{mean}}^A = \frac{\sum_{i=1}^m (N_i \cdot D_i^2) D_i}{\sum_{i=1}^m N_i \cdot D_i^2} = \sum_{i=1}^m f_i^A \cdot D_i, \quad [1]$$

where  $N_i$ ,  $D_i$ , and  $f_i$  are the number of grains, the average diameter, and the area fraction of each class  $i$ , respectively. For comparison, the mean diameter calculated from classic arithmetic mean  $D_{\text{mean}}^N$  is also reported:

$$D_{\text{mean}}^N = \frac{\sum_{i=1}^m (N_i \cdot D_i)}{\sum_{i=1}^m N_i} = \sum_{i=1}^m f_i^N \cdot D_i. \quad [2]$$

**Table I. Mean Composition (in Weight Percent) of MA Powder and the Consolidated SPS Sample at 1423 K (1150  $^{\circ}\text{C}$ ) Measured by Electron Microprobe**

Element	Fe	Cr	W	Y	O	Ti	Si
Powder (ref.)	bal.	14.6 $\pm$ 0.1	0.99 $\pm$ 0.02	0.16 $\pm$ 0.02	0.15 $\pm$ 0.01	0.32 $\pm$ 0.02	0.19 $\pm$ 0.01
Compact sample	bal.	14.5 $\pm$ 0.1	1.01 $\pm$ 0.02	0.16 $\pm$ 0.02	0.15 $\pm$ 0.06	0.32 $\pm$ 0.03	0.18 $\pm$ 0.01

## 2. Electron microprobe analysis

At microscale, chemical homogeneity of both MA powder and sintered samples was characterized by electron probe microanalysis using a device SX 100 CAMECA. Samples were mechanically polished with a finishing using Silica suspension solution. The column conditions were a voltage of 15 kV and a current of 100 nA.

## 3. Small-angle neutron scattering (SANS)

SANS experiments were performed at the Laboratoire Léon Brillouin CEA Saclay, using the PAXY small-angle scattering spectrometer for high resolution in  $q$ -space, under strong magnetic field (1.7 T). As mentioned in Reference 26, a magnetic field of magnitude 1.2 T is sufficient to separate the magnetic and nuclear contributions. SANS experiments were set to determine the distribution of particles smaller than 15 nm in radius. This corresponds to a scattering vector  $q$  between 0.1 and 1.6 nm<sup>-1</sup>. This was obtained by selecting neutron wavelengths of 0.6 and 1 nm ( $\pm 10$  pct due to monochromator dispersion) and a distance between sample and detector of 2 and 5 m, respectively. A 2D detector with area 64 × 64 cm<sup>2</sup> was used to collect scattered neutrons. Recently, the technique has emerged as a powerful tool for nanoscale characterization of ODS steels, often associated to TEM analysis.<sup>[4,22,26]</sup> As detailed in Reference 27, a direct modeling was used in the current study. The scattering function was calculated for a given distribution of nano-scatterers and compared to the experimental function. A least squares method was used to obtain the best fitting parameters. The particles were assumed spherical—as demonstrated experimentally in Ti-added ODS steels<sup>[28]</sup>—and of constant chemical composition. Particle mean radius  $r_m$  of the scattering population was calculated assuming a normalized number density function of radii  $h(r)$ . Given these assumptions, one can write the scattering intensity as:

$$I(q, r) = \Delta\rho^2 N_p V_p^2 F_{\text{sph}}(q, r) S(q, r), \quad [3]$$

where  $N_p$  is the scatterers density,  $V_p$  the volume of a scattering particle,  $\Delta\rho$  the difference of diffusion length densities between the matrix and the scatterers.  $F_{\text{sph}}(q, r)$  is the shape factor for spheres:

$$F_{\text{sph}}(q, r) = \left[ 3 \frac{\sin(qr) - qr \cos(qr)}{(qr)^3} \right]^2 \quad [4]$$

$S(q, r)$  is the structure factor resulting from the particles interaction. If the volume fraction of precipitates is observed to be less than 1 pct (diluted system),  $S(q, r)$  tends to 1. A Gaussian distribution of spherical particles was chosen for direct modeling:

$$h(R) = \frac{1}{\sigma\sqrt{2\pi}} e^{-\frac{(r-R_m)^2}{2\sigma^2}}. \quad [5]$$

Considering that the matrix is ferromagnetic, one can verify the global chemical composition of the nano-scattering particles by decoupling the nuclear and

magnetic contrasts.<sup>[4,27]</sup> Indeed, the scattering ratio  $A$  is given by:

$$A = 1 + \left( \frac{\Delta\rho_M}{\Delta\rho_N} \right)^2, \quad [6]$$

where  $\Delta\rho_M$  and  $\Delta\rho_N$  are the magnetic and nuclear contrasts, respectively. Regarding ODS steels, the ratio  $A$  depends upon the composition of the steel and the nature of the oxides. In Fe-14Cr steel, typical values are 2.5 for pyrochloric structure  $Y_2Ti_2O_7$  and 3.2 for cubic  $Y_2O_3$ , as demonstrated in Reference 27.

## III. THEORY AND CALCULATION

In ODS steels and particularly in the current study, the grain structure is heterogeneous and exhibits strong thermal stability. To understand how this specific microstructure can form and why it shows significant resistance to grain growth, one needs to understand and quantify which mechanisms are involved and what are the main driving/dragging pressures that compete in governing the microstructure. The latter are described in Section III–A. Then, Section III–B describes the Kernel average misorientation (KAM) as an experimental tool to measure the stored energy in deformed materials.

### A. Driving Pressures for Recrystallization and Grain Growth

The Gibbs free energy of a system composed of two grains A and B separated by a grain boundary is given by:

$$G = g_A V_A + g_B V_B + \gamma S, \quad [7]$$

where  $g_A$  and  $g_B$  are the volume Gibbs free energy,  $V_A$  and  $V_B$  are the volume of the grain A and B,  $\gamma$  the grain boundary energy, and  $S$  the grain boundary surface. The driving pressure for grain growth is derived from the energy gradient through the grain boundary that can be written as:

$$P = -\frac{dG}{dV} = (g_b - g_a) + \gamma \frac{dS}{dV} = P_v + P_c. \quad [8]$$

- (i) The driving pressure for recrystallization due to the difference in stored energy between each side of a grain boundary can be written as:

$$P_v = aGb^2(\rho_b - \rho_a) \quad [9]$$

where  $G$  is the shear modulus,  $b$  the Burgers vector magnitude, and  $\rho_a$  and  $\rho_b$  the dislocation density in the grain A and B, respectively.

- (ii) Assuming spherical grains, the capillary driving pressure for grain growth is described as:

$$P_c = \gamma \frac{dS}{dV} = \gamma \frac{8\pi R dR}{4\pi R^2 dR} = \frac{2\gamma}{R}, \quad [10]$$

where  $R$  is the mean radius of the grain. Typical values of grain boundary energies are 0.2 J m<sup>-2</sup> for

low-angle grain boundary and  $0.5 \text{ J m}^{-2}$  for high-angle grain boundary.<sup>[29]</sup> Calculations of this pressure are reported in Table II, considering three types of grains: ultra-fine grains ( $R_1 = 0.2 \mu\text{m}$ ), micron grains ( $R_2 = 2 \mu\text{m}$ ), and coarse grains ( $R_3 = 20 \mu\text{m}$ ). The dragging pressure impeding the grain growth is due to heterogeneities that consist of obstacles for solvent atom diffusion. They can be solute atoms that can either segregate at grain boundaries, or form second-phase particles with full, partial, or no coherency with the matrix.

- (iii) The solute drag effect is due to solute atoms (impurities) that reduce grain boundary migration.<sup>[30]</sup> The lowered mobility  $M'$  is dependent on the solute concentration:

$$M' = \left( \frac{1}{M_{\text{pure}}} + \alpha_{\text{drag}} X_i \right)^{-1} \quad [11]$$

where  $\alpha_{\text{drag}}$  is temperature dependent and therefore defined by an activation energy,  $X_i$  the solute concentration. For instance, Cram *et al.*<sup>[31]</sup> evaluated the influence of tin content in pure copper and highlighted that the solute effect is considerable at low temperature but much less effective at higher temperature. In the current study, the solute effect was neglected due to the considered temperature range.

- (iv) If solute diffusion is high enough and miscibility low enough to form second-phase particles, the latter can induce a pinning effect, whose efficiency is related to their distribution.<sup>[32]</sup> The influence of this particles dispersion on grain boundary mobility can be modeled using a tough boundary.<sup>[33]</sup> The resulting pressure exerted by a particle distribution is then:

$$P_Z = \frac{3}{2} \gamma \frac{f_p}{r_p}, \quad [12]$$

where  $f_p$  and  $r_p$  are the volume fraction and mean radius of the precipitates, respectively. The maximum size that a grain can reach is defined by an equilibrium state where driving pressure and pinning pressure are equal:

$$R_c = C \frac{r_p}{f_p}, \quad [13]$$

where  $C$  is a constant depending upon the hypothesis.<sup>[34]</sup>

Considering typical microstructural features that are described in the next section (grain size, dislocation density, precipitation state), the driving and dragging pressures for grain growth were calculated using Eqs. [9], [10], [12] and reported in Table II. Grain boundary energies are taken  $0.2 \text{ J m}^{-2}$  for ultra-fine grains (UFG) and  $0.5 \text{ J m}^{-2}$  for coarse grains because UFG were found to be surrounded by low-angle grain boundaries (LAGB) whereas coarse grains by high-angle grain boundaries.

$\Delta\rho$  was assumed to be equal to the average dislocation density, meaning that influence of dislocation density in recrystallized grains was neglected. Pinning pressure was calculated assuming a volume fraction of 1 pct of precipitates of three different radii, 2 nm corresponding to the nanoparticles measured by SANS. The critical grain sizes were calculated using Eq. [13]. This evaluation was used to advance a scenario detailed in Section V.

## B. Study of Recovery and Recrystallization by Kernel Average Misorientation

Deforming a metal generates a drastic change of properties due to the increased number of defects in the material that make it unstable. Dislocations have significant influence on the behavior of a deformed

**Table II. Driving and Pinning Pressures Governing Grain Growth**

Capillary Pressure		(i) Capillary Effect			
Experimental internal variables (inputs)	grain radius ( $\mu\text{m}$ )	$5 \times 10^{-2}$	$2 \times 10^{-1}$	2	20
	grain boundary energy $\gamma$ ( $\text{J m}^{-2}$ )	0.2	0.2	0.5	0.5
Calculation output:	capillary pressure $P_C$ (MPa)	8	2	$5 \times 10^{-1}$	$1 \times 10^{-2}$
Driving pressure		(ii) Stored Energy Effect			
Experimental internal variable (input)	variation of dislocation density $\Delta\rho$ ( $\text{m}^{-2}$ )	$10^{16}$	$10^{15}$	$10^{14}$	$10^{13}$
Calculation output:	driving pressure $P_V$ (MPa)	23	2.3	$2.3 \times 10^{-1}$	$2.3 \times 10^{-2}$
Pinning Pressure		(iii) Pinning Effect			
Experimental internal variables (inputs)	precipitate radius (nm)	2	20	200	
	volume fraction	$10^{-2}$	$10^{-2}$	$10^{-2}$	
Calculation outputs:	critical grain size ( $\mu\text{m}$ ) (where $C = 4/3$ <sup>[33]</sup> )	$2.7 \times 10^{-1}$	2.7	27	
	critical grain size ( $\mu\text{m}$ ) (where $C = 1/6$ <sup>[34]</sup> )	$3.4 \times 10^{-2}$	$3.4 \times 10^{-1}$	3.4	
	pinning pressure $P_Z$ (MPa)	3.8	$3.8 \times 10^{-1}$	$3.8 \times 10^{-1}$	

Calculations of  $P_C$ ,  $P_V$ , and  $P_Z$  are independent and performed using typical microstructural features measured on either as-milled powder or consolidated materials (SPS and HIP).

metal during subsequent annealing or thermo-mechanical treatment. Consequently, various methods to measure the stored energy have been used for the last decades. Dislocations density can be derived by calorimetry for some metals with well-known stacking fault energy.<sup>[35,36]</sup> Yet, annealing behavior of a deformed metal does not only depend upon the overall stored energy but more importantly on its spatial distribution, especially in heterogeneous grain structure. On a local scale, inhomogeneity of stored energy will affect the onset of recrystallization, and larger scale heterogeneity will influence the growth of the new grains. Recently, EBSD technique has emerged as a powerful tool for determining an orientation map within a grain structure.<sup>[37]</sup> This permits to highlight local metallurgical heterogeneities such as specific orientation gradient, for instance at phase boundaries in dual-phase steels<sup>[37]</sup> or after mechanical testing on ODS Fe-9Cr alloys.<sup>[38]</sup> In the current study, the KAM has been calculated from EBSD orientation maps. The KAM evaluates the mean misorientation of a pixel based on the comparison of the orientation of  $n$  layers of neighboring pixels that constitute a Kernel. Misorientations above a certain value—2 or 5 deg are standard thresholds—are excluded in order to avoid the influence of grain boundaries. Only the first layer of neighboring

pixels has been considered in this calculation. For each pixel  $i$  surrounded by  $n$  pixels, the KAM value is given by:

$$\theta_i^{\text{KAM}} = \frac{1}{n} \sum_{j=1}^n \Delta\theta_{ij} \quad [14]$$

where  $\Delta\theta_{ij}$  represents the misorientation between the pixels  $i$  and  $j$ . Contrary to the global mean misorientation of a grain, which is defined by the mean misorientation between every pixel constituting the whole grain, the KAM does not depend on the grain size. Thus, this gives pertinent information for the study of local heterogeneity. The KAM can be related to the geometrically necessary dislocations density (GND) to accommodate plastic deformation using the equation:<sup>[37,39,40]</sup>

$$\rho(\text{GND}) = 2\theta_m^{\text{KAM}}/ub, \quad [15]$$

where  $\theta_m^{\text{KAM}} = \sum_{i=1}^P \theta_i^{\text{KAM}}$  is the average misorientation

calculated by KAM in radians,  $b = 0.248$  nm the Burgers vector in ferrite, and  $u$  the unit length defined by  $u = na$  if  $n$  is the number of neighbors layer and  $a$  the EBSD step size. In opposition to the KAM, dislocation density does not depend upon the acquisition parameters.

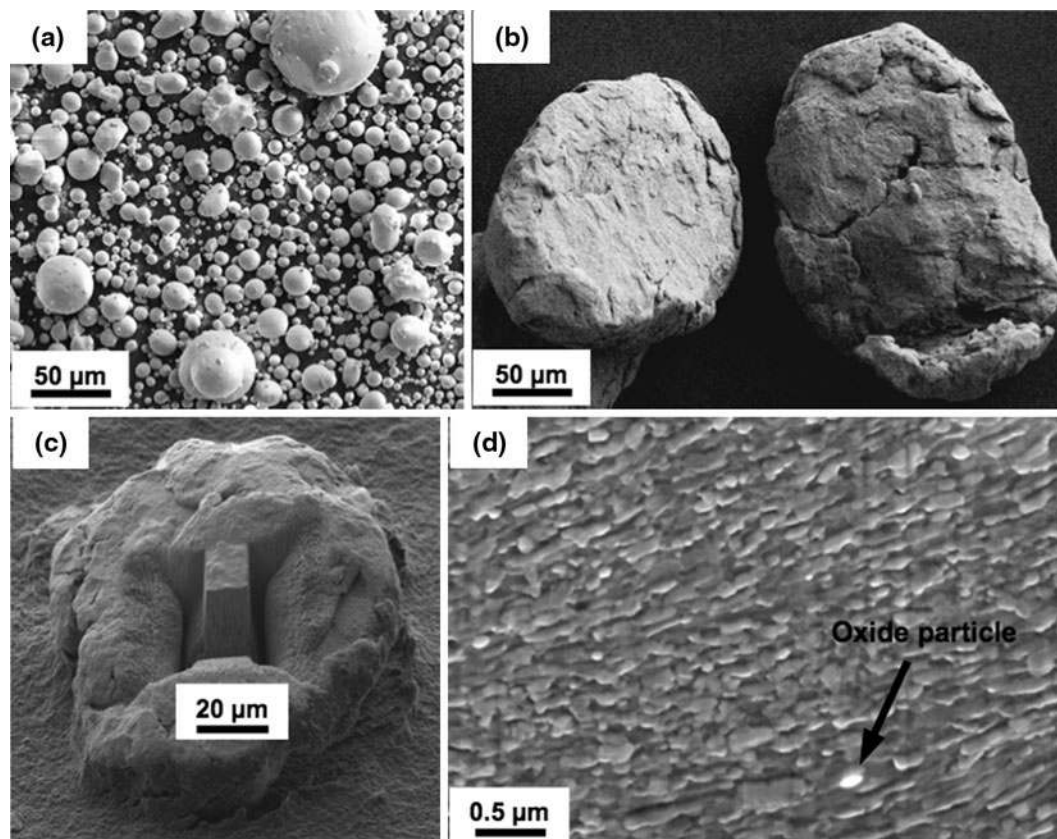


Fig. 1—(a) Atomized Fe-14Cr powder, (b) mechanically alloyed powder, (c) powder particle milled by focused ion beam (FIB) cross-sectioning, (d) corresponding SEM-FEG image of the nanosized grain structure.

## IV. EXPERIMENTAL RESULTS

In this section, the as-milled powder is described first. Then, the multiscale characterization of ODS materials processed by SPS/HIP is presented in Section IV–B.

### A. As-milled Powder

As microstructural and mechanical properties of compacts strongly depend upon the original nanostructure, it is of prime importance to characterize the initial grain structure before sintering. The as-atomized powder particles are spherical with an average diameter of  $70\ \mu\text{m}$  (Figure 1(a)). After mechanical alloying (MA), the particles are highly deformed, describing stratified cold-welded structure with an angular shape (Figure 1(b)). In order to characterize the deformed microstructure, powder particles were milled by Focused Ion Beam (Figure 1(c)) and characterized by EBSD using a SEM-FEG with resolution down to  $10\ \text{nm}$ . Figure 1(d) illustrates the nanostructure observed on a cross-section. A few particles enriched in yttrium and oxygen were scarcely dispersed in the powder, as illustrated in Figure 1(d). These phases are most likely remaining fragments of yttria particles that were introduced into the ferritic matrix during MA but not fully dissolved into solid solution. The heterogeneous nanostructure is reported in Figure 2(a), where black pixels correspond to the most cold-worked grains that could not be indexed. The grain size distribution is wide, with ultra-fine grains from  $50$  to  $800\ \text{nm}$ , defining a mean diameter of  $250\ \text{nm}$ .

### B. Consolidated Materials

In this section, the evolution of the microstructure during consolidation by SPS and HIP and after heat-treating at  $1373\ \text{K}$  ( $1100\ ^\circ\text{C}$ ) is described. Grain growth is reported in Section IV–B–1, the annealing behavior in Section IV–B–2, and precipitation in Section IV–B–3.

#### 1. Grain growth

As temperature drastically influences grain growth, SPS cycles were performed at different soaking temperatures at a constant dwell time fixed at  $5$  minutes. The heating rate was  $8.3\ \text{K s}^{-1}$  ( $500\ \text{K min}^{-1}$ ). Figure 2 illustrates the evolution of the microstructure as a function of SPS soaking temperature, then during further annealing. Figure 2(f) also describes the microstructure of the HIPed sample. The microstructure of the compact SPSed at  $1123\ \text{K}$  ( $850\ ^\circ\text{C}$ ) is composed of isotropic grains from  $50\ \text{nm}$  to around  $1\ \mu\text{m}$  for the largest ones (Figure 3(b)), which is very close to what was observed on the as-milled powder. At this state, the structure is composed of ultra-fine grained zones where subgrains of same or close orientation are surrounded by LAGB. Primary recrystallization may occur around this temperature.

When considering the grain structure of the sample SPSed at higher temperatures [ $T = 1323\ \text{K}$  or  $1423\ \text{K}$  ( $1050\ ^\circ\text{C}$  or  $1150\ ^\circ\text{C}$ )], there is no evidence of large grains with equivalent orientation. Thus, the large recrystallized grains do not form from the substructured grains but more likely from new nuclei with random orientation. Moreover, ultra-fine grains or substructured grains are very stable in size, although they

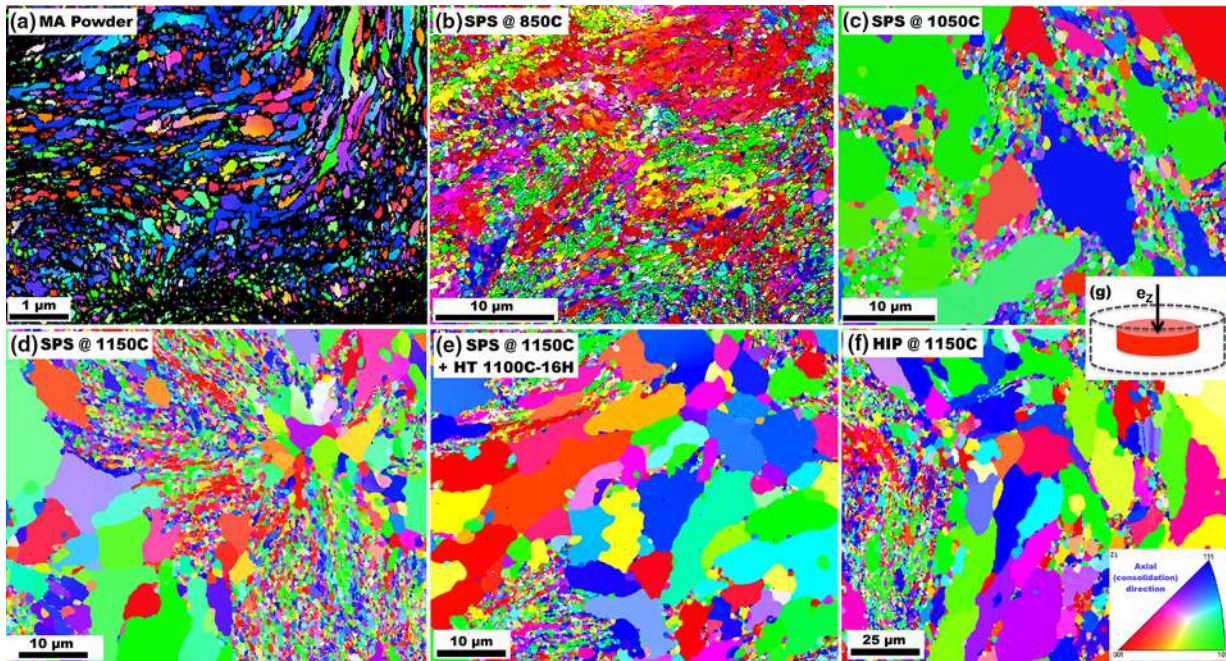


Fig. 2—(a) EBSD maps of as-milled powder, (b) SPSed ODS at  $1123\ \text{K}$  ( $850\ ^\circ\text{C}$ ), (c) at  $1323\ \text{K}$  ( $1050\ ^\circ\text{C}$ ), (d) at  $1423\ \text{K}$  ( $1150\ ^\circ\text{C}$ ), (e) SPSed at  $1423\ \text{K}$  ( $1150\ ^\circ\text{C}$ ) and heat treated at  $1373\ \text{K}$  for  $16\ \text{h}$ , (f) HIPed ODS at  $1423\ \text{K}$  ( $1150\ ^\circ\text{C}$ )— $e_z$  is the axial direction during SPS/HIP consolidation.

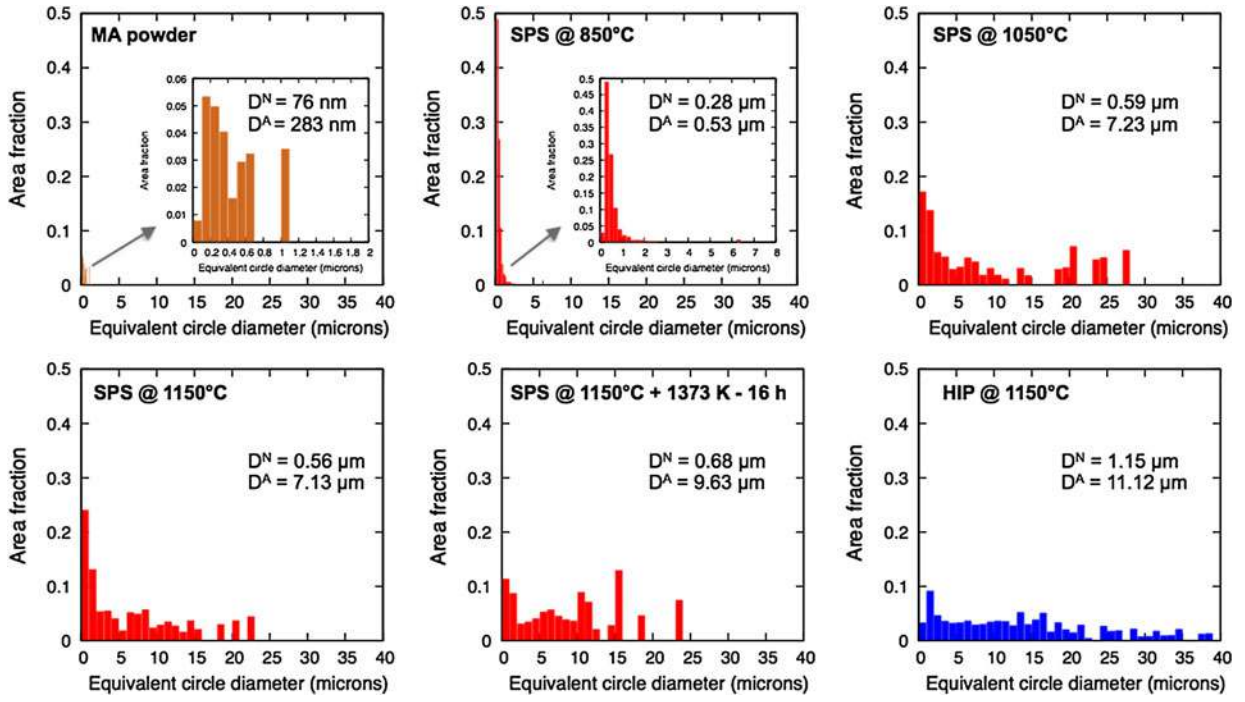


Fig. 3—Grain size distribution in area fraction determined from the EBSD maps of (a) as-milled powder, (b) ODS steels SPSed at 1123 K (850 °C), (c) at 1323 K (1050 °C), (d) at 1423 K, (e) SPSed at 1423 K then annealed at 1373 K for 16 h and (f) HIPed at 1473 K.

represent a much lower volume fraction after high-temperature SPS processing. From 1323 K (1050 °C), the grain size distribution drastically broadens, with the largest grains reaching an equivalent circle diameter of 20 to 25  $\mu\text{m}$ .

This distribution is comparable to that of the SPSed compact processed at 1423 K (1150 °C), showing a certain stability of the grain structure within the temperature range 1323 K to 1423 K (1050 °C or 1150 °C), with no significant growth of the smallest grains that seem to be still stable at these temperatures. These results point out the reproducibility of such structure, which is necessary to justify when seeking good and repeatable mechanical properties. When looking at the sample SPSed at 1423 K (1150 °C) subsequently treated at 1373 K (1100 °C) (roughly equal to 0.8 times the solidus temperature for steels) for 16 hours, the grain size distribution indicates that (i) the smallest grains keep showing a strong resistance to coarsening, (ii) the critical size of the largest grains does not increase whereas their volume fraction increases. These observations illustrate that pinning has an efficient effect on the whole grain structure. Finally, the HIPed material contains a higher volume fraction of coarse grains, demonstrating the benefit of short SPS treatments (Table III).

## 2. Recovery study using Kernel average misorientation

As MA is well known to introduce huge amount of plastic work into the milled powder, one can expect a strong influence of the stored energy on the microstructural behavior during hot consolidation. This section describes how the KAM was used to characterize the

spatial distribution of this stored energy and how it annihilated during hot processing. The linear relationship between KAM and dislocation density (Eq. [15]) allows a direct comparison between deformation levels within the same EBSD map. Thus, the evolution of the stored energy was measured on different metallurgical states depending upon the consolidation temperature, which is reported in Figure 4. First of all, the MA powder contains various levels of plastic deformation. Some grains are poorly deformed whereas the major part of the nanosized grains underwent drastic cold work, which are the unindexed grains (black areas). The kinetics study clearly shows that some grains are already recovered at 1123 K (850 °C) whereas some others are still deformed.

Above 1373 K (1100 °C), the large recrystallized grains show very limited local misorientation. The major part of the local misorientation is contained in ultra-fine-grained zones with low-angle grain boundaries. The GND was derived for each microstructure from the whole KAM distribution, as shown in Figure 5(a). GND drops from  $1 \times 10^{16} \text{ m}^{-2}$  for the as-milled powder to  $1 \times 10^{15} \text{ m}^{-2}$  for the ODS SPSed at 1423 K (1150 °C). This decrease of only one order of magnitude is expected to be due to dislocations recovery. GND logically decreases with consolidation temperature. The comparison between SPS and HIP shows higher volume fraction of recrystallized grains, which highlight the effect of heating rate during consolidation. This kinetic effect is exacerbated in SPS consolidation because very fast heating induces partial appearance of thermally activated phenomena, such as recovery mechanisms. Thus, a plateau value of  $(5 \pm 2) 10^{14} \text{ m}^{-2}$  is

**Table III. Mean Grain Size Calculated from Area and Number Fractions for as-Milled, SPSed, SPSed and Annealed at 1373 K (1100 °C), and HIPed ODS Samples**

Processing	SPS					HIP 1423 K (1150 °C)
	MA Powder	1123 K (850 °C)	1323 K (1050 °C)	1423 K (1150 °C)	1423 K (1150 °C)	
Annealing	—	—	—	—	+ HT 1373 K (1100 °C)—1 h	—
$D_{\text{mean}}^N$ ( $\mu\text{m}$ )	0.08	0.28	0.59	0.56	0.57	1.15
$D_{\text{mean}}^A$ ( $\mu\text{m}$ )	0.28	0.53	7.23	7.13	7.45	11.12

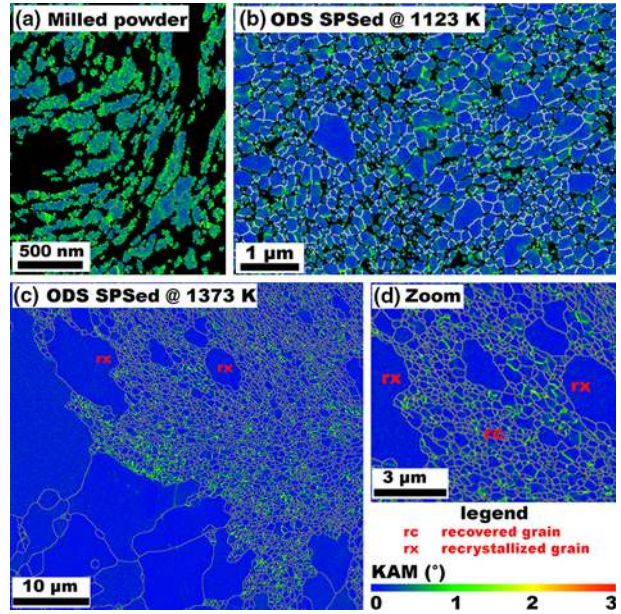


Fig. 4—Evolution of local intragranular misorientation from (a) milled powder to (b) ODS processed by SPS at 1123 K (850 °C) and (c, d) at 1373 K (1100 °C). Unindexed black areas and green dots highlight the local concentration of plastic deformation. Blue grains are completely recrystallized. (c, d) illustrate the evidence of entire recovery in small grains around large recrystallized grains, lowering the difference in stored energy (Color figure online).

reached on a SPSed compact annealed at 1373 K (1100 °C) for 16 hours, versus  $1.4 \times 10^{14}$  ( $\pm 5 \times 10^{13}$ )  $\text{m}^{-2}$  for the HIPed materials. Competing recovery and recrystallization of the grain structure play a role on this reduction. Large recrystallized grains have low dislocation density when ultra-fine grains contain non-negligible amount of stored energy.<sup>[41]</sup> These areas are defined by a network of LAGB. The stability of such subgrain boundaries has been assessed with a heat treatment at 1373 K (1100 °C) for 16 hours. The extreme stability of the grain structure is highlighted in Figure 5(b). One can notice the network of LAGB within the UFG when large grains are uniquely separated by high-angle grain boundaries (HAGB).

### 3. Precipitation

Analyses by SEM-FEG for coarse oxides and by small-angle neutron scattering for nanosized precipitates were carried out. The precipitation state is composed of at least two types of particles.

Ti-enriched oxides from 50 to 250 nm in diameter were observed in both the SPSed and HIPed materials at grain boundaries but mainly in the largest grains (Figure 6). Electron microprobe analysis showed Ti-O enriched lines, the major part of which had no yttrium content. The typical distance between precipitates lines is 10 to 70  $\mu\text{m}$ , which corresponds to the size range of MA powder particles. This emphasizes the influence of topology in powder metallurgical microstructure, especially coarse precipitation.<sup>[16]</sup> This was confirmed by Sakasegawa *et al.*<sup>[42]</sup> from TEM replicas on an ODS steel of composition Fe-14Cr-1.0Ti-0.25Y<sub>2</sub>O<sub>3</sub> (in

wt pct). Other coarse oxides of more than 50 nm in diameter were also found by de Castro *et al.*<sup>[43]</sup>: Al-Y-O, Cr<sub>2</sub>O<sub>3</sub>, and Y-Cr-V-O. These coarser particles may have two consequences: (i) the decrease of titanium and oxygen contents available for nanoparticles precipitation, therefore the decrease in volume fraction of nanosized oxides, (ii) a potential pinning effect depending upon the size and number density of the coarse particles, which will be discussed in the next section.

Nanoparticles, having a mean diameter of 3.2 nm, were detected by small-angle neutron scattering (Figure 7(a)). They were also measured in HIPed materials, as reported in Table IV. This highlights the importance of adding titanium to refine the distribution, as demonstrated by Ukai and confirmed by Ratti.<sup>[1,44]</sup> Furthermore, although a slight decrease in number density is observed with increased processing time, the mean volume fraction of detected nanoparticles is constant

and equal to 1 pct. The volume fraction for SPSed ODS at 1323 K and 1423 K (1050 °C and 1150 °C) for 5 minutes is overestimated, as the theoretical maximum volume fraction of Y<sub>2</sub>Ti<sub>2</sub>O<sub>7</sub> would be 0.9 pct. Local enrichment in oxygen, iron or chromium could explain higher volume fraction detected by SANS.<sup>[4]</sup> In this sense, atom-probe tomography would be necessary to quantify the composition of the nanoparticles.

The scattering *A*-ratio (Eq. [6]) measured in SPSed and HIPed ODS steels was constant and equal to 2.3. This value is fairly consistent with Y-Ti-O complex nanoparticles. For instance, in a ferritic steel hot isostatically pressed at 1423 K (1150 °C), Alinger *et al.*<sup>[4]</sup> determined a ratio of 2.04 and 2.60 for Y<sub>2</sub>Ti<sub>2</sub>O<sub>7</sub> and Y<sub>2</sub>TiO<sub>5</sub>, respectively. The value of *A* depends on the atomic volume, thus on the crystallographic structure. The latter was assumed to be of pyrochlore type, as referred in Reference 28. Various studies by transmis-

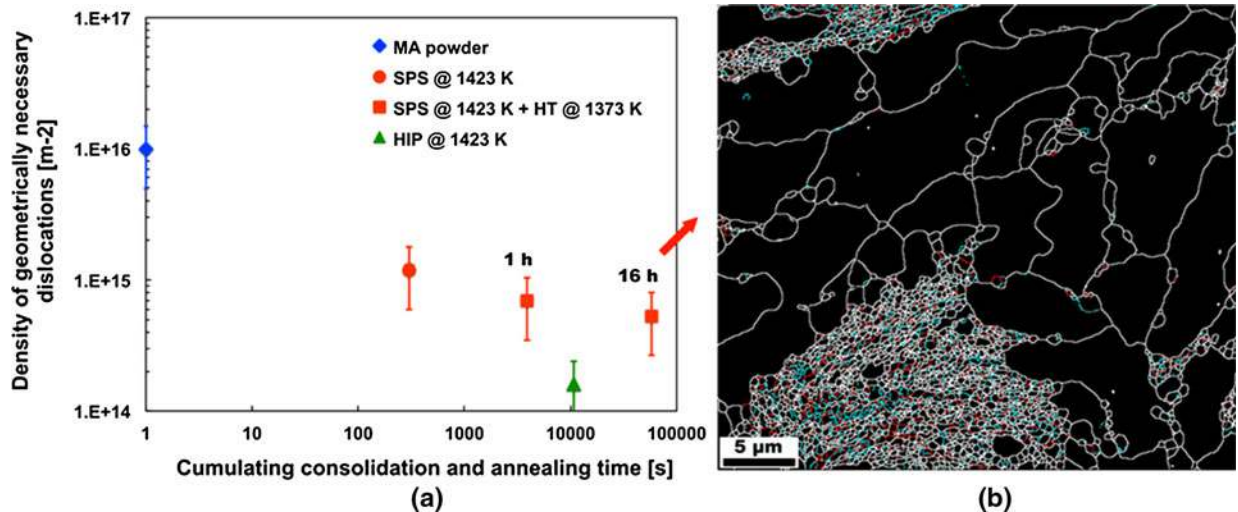


Fig. 5—(a) Dislocations density according the cumulated processing time at 1423 K (1150 °C) and annealing time at 1373 K (1100 °C). The plotted points correspond to the mean value of two measurements for each state. Even if the highest standard deviation (obtained on the milled powder) was 32 pct, more conservative error bars were set at 50 pct. (b) Grain boundaries measured by EBSD [blue: 2 to 6 deg; red: 6 to 10 deg; white: over 10 deg] on a sample SPSed at 1423 K (1150 °C) then annealed at 1373 K (1100 °C) for 16 h (Color figure online).

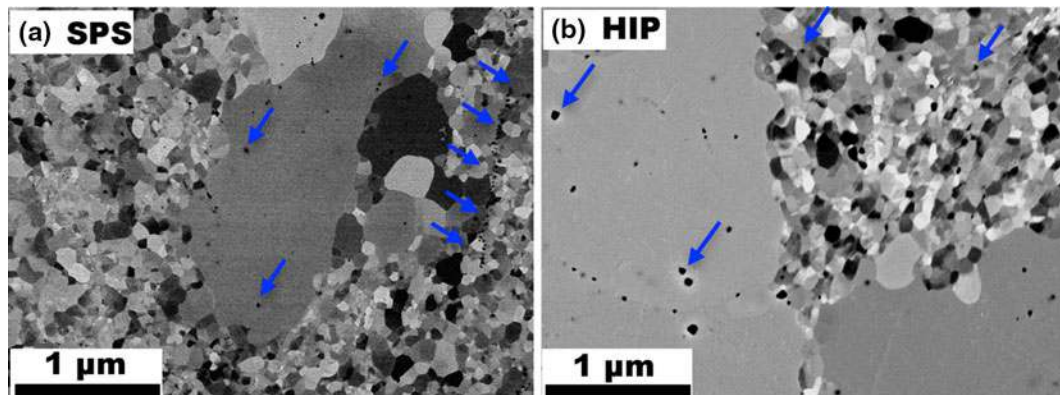


Fig. 6—SEM-FEG images (BSE mode) of ODS steels (a) SPSed at 1423 K (1150 °C) and (b) HIPed at 1423 K (1150 °C). This reveals coarse oxides (black dots) within the large grains.

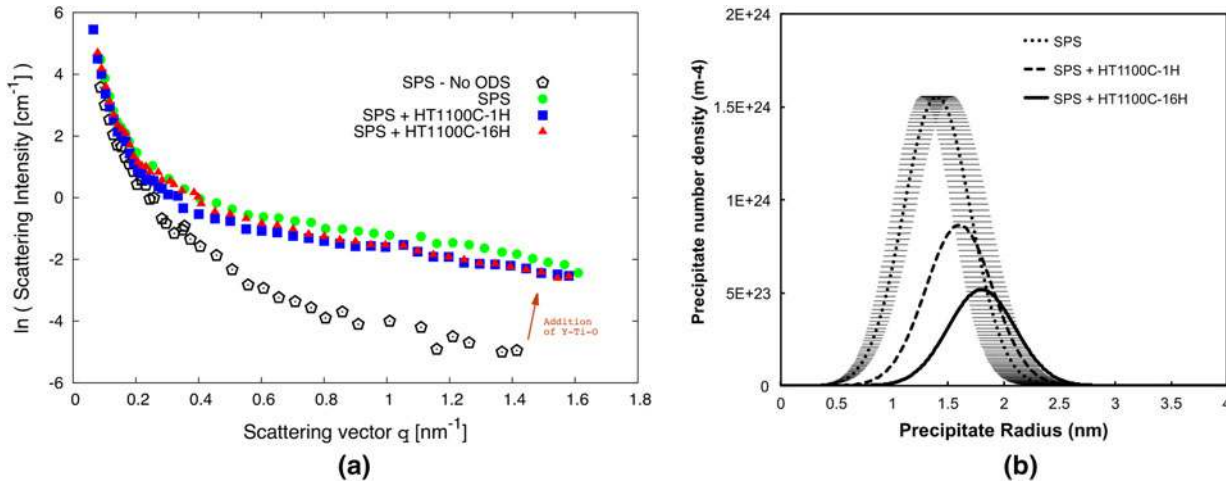


Fig. 7—(a) Magnetic scattering intensity measured by small-angle neutron scattering on samples SPSed at 1423 K (1150 °C) and then annealed at 1373 K (1100 °C) and (b) the corresponding nano-oxides distribution in number density. Horizontal errors bars in (b) take into account the uncertainty of 10 pct in  $r_m$  due to direct fitting.

Table IV. Nanoparticles Detected by Small-Angle Neutron Scattering

Consolidation Parameters			Annealing		$r_m$ (nm)	$\sigma$ (nm)	$f_v$ (Percent)	A-Ratio
SPS	1423 K (1150 °C)	5 min	—	—	1.4	0.3	$1.54 \pm 0.4$	2.3
			1373 K (1100 °C)	1 h	1.6	0.3	$1.03 \pm 0.2$	2.3
			1373 K (1100 °C)	16 h	1.8	0.3	$1.03 \pm 0.2$	2.3
HIP	1423 K (1150 °C)	3 h	—	—	1.6	0.2	$1.14 \pm 0.2$	2.3
			1373 K (1100 °C)	1 h	1.6	0.3	$1.03 \pm 0.2$	2.3
			1373 K (1100 °C)	16 h	1.6	0.4	$1.14 \pm 0.2$	2.3

sion electron microscopy,<sup>[42,45–47]</sup> atom-probe tomography,<sup>[23]</sup> or small-angle neutron scattering<sup>[4,27]</sup> report at least two kinds of nanoparticles:

- Complex Fe-Cr-Y-Ti-O non-stoichiometric nanoclusters ( $d \sim 2$  nm) that are fully coherent within the bcc matrix
- Nanosized oxides ( $d \sim 5$  to 15 nm), mainly having a pyrocholoric structure composed of  $Y_2Ti_2O_7$  even if  $Y_2TiO_5$  have been observed as well.<sup>[48]</sup>

## V. DISCUSSION

Grain growth and precipitation are strongly linked in complex systems such as ODS steels. Appearance of heterogeneous grain structure, as described in this current study, has been often reported. Second-phase particles are known to strongly pin either grains or subgrains. Although numerous on-going studies clearly report the extreme stability of the oxides with less than 10 nm in diameter, other larger particles were found in the sintered materials. The composition of these “coarse” oxides has a high content in titanium and oxygen. Such coarse precipitation, mainly at grain boundaries, is most likely due to:

- (i) initial chemical inhomogeneity within the as-milled powder particles. Even nowadays high-energy

milling is known to be efficient enough to produce homogeneous ODS powder, one should keep in mind that a perfect solid solution of several kilograms in batch production is difficult to achieve. Besides, the oxygen content has been reported by Williams *et al.*<sup>[23]</sup> to come from contamination during consolidation, rather than from the yttria powder itself. They introduced either  $FeY_2$  or  $Y_2O_3$  with no relevant change in oxygen content in the consolidated materials.

- (ii) A large gap between titanium and oxygen diffusion coefficients with respect to that of other solutes, such as yttrium, and tungsten.

Due to their size, these large particles most likely have a weak pinning effect (Table II). Thus, grain boundaries may surround these particles with no drastic change in their mobility. This is why they are mainly localized in large grains. Using the same criteria, one can explain the extreme stability of UFGs pinned by nanosized particles. The latter have been observed to delay the onset of recrystallization of mechanically alloyed iron-base and nickel-base alloys.<sup>[49]</sup> Bhadeshia suggested that triple-junction pinning might stabilize these alloys. In addition to basic pinning due to geometrical interaction between grain boundary and particles, an effect of topology was emphasized.

The grain structure of SPSed ODS steels may be explained by the following scenario:

(a) The initial nanostructure contains highly deformed ultra-fine grained zones. The stored energy due to plastic work is considerable and somehow inhomogeneous in a powder particle. Thus, the driving pressure for recrystallization is significant (above 20 MPa; Table II). Heterogeneous, competing recovery, and recrystallization occur when heating the material. At moderate temperatures during SPS/HIP consolidation [ $T < 1123$  K (850 °C)], substructures may be annealed to form dislocation-free subgrains. Stored energy of recovered cells, consequently the driving pressure for grain boundary mobility, are sharply decreased. This induces exceptional stability of ultra-fine grains.

Simultaneously, new grains nucleate on favorable sites such as plastically strained zones. Since there is a significant difference in stored energy between clean nuclei and their deformed and unrecovered neighbors, grain boundaries of recrystallized grains are highly mobile, which favors their growth at the expense of the deformed ones. This mechanism can be much quicker than dislocation recovery. Moreover, temperature gradient effects may enhance this discontinuous evolution. Grains located at the powder particle upper shell have a higher probability to recrystallize, as local temperature gradients can be generated by reactive heating at free surfaces in the SPS furnace. Indeed, Ji *et al.*<sup>[6]</sup> argued that this effect could be responsible for the onset of recrystallization within a Fe-Al alloy. Yet, the current study demonstrates that the hypothetical SPS heating effect must be moderate because the heterogeneous recrystallization was observed on HIPed materials as well.

(b) At higher temperature [ $T = 1123$  to 1423 K (850 °C to 1150 °C)], precipitation occurs. Grain

boundaries and dislocations are favorable sites for nucleation.<sup>[50–52]</sup> De Castro *et al.*<sup>[43]</sup> observed heterogeneously distributed unrecovered zones where dislocations and nanoparticles were numerous. The number density of nano-oxides is high enough to induce precipitation in the bulk as well. Both UFG and large grains contain nanoparticles. Oxides pinning effect is efficient enough to annihilate the subgrain mobility in UFG. Thus, the subgrain growth mechanism inducing large grains is excluded.<sup>[53]</sup> In this study, pinning pressure was not decreased due to limited coarsening of nanoparticles (Table II), as observed by others.<sup>[43]</sup> Indeed, thermal stability of nanoparticles can be extreme in ODS steels, as they do not coarsen at temperatures up to  $0.8 T_s$ , with  $T_s$  being the solidus temperature of the alloy. The mean diameter of the nanoparticles was 3.2 nm after annealing of the SPSed materials at 1373 K (1100 °C) for 16 hours. Such stability can be explained by a full lattice coherency between the ferritic bcc matrix and nanoparticles that decreases the interface energy and consequently boosts the oxides' stability.<sup>[28,54]</sup> Coarse particles ( $d > 50$  nm) were also observed, but their contribution to pinning is much lower. Once precipitation has occurred, one can expect the capillary driving pressure and the pinning pressure to compete with each other. If considering the pinning effect induced by the nanoparticles with a volume fraction of 1 pct, the pressure is high enough (3.8 MPa; Table II) to impede grain growth (Figure 8). However, a quantitative study of grain boundary mobility in ODS steels is still lacking. Measurement of grain boundary mobility can be done by determining the velocity of boundaries in a well-known system with constant driving pres-

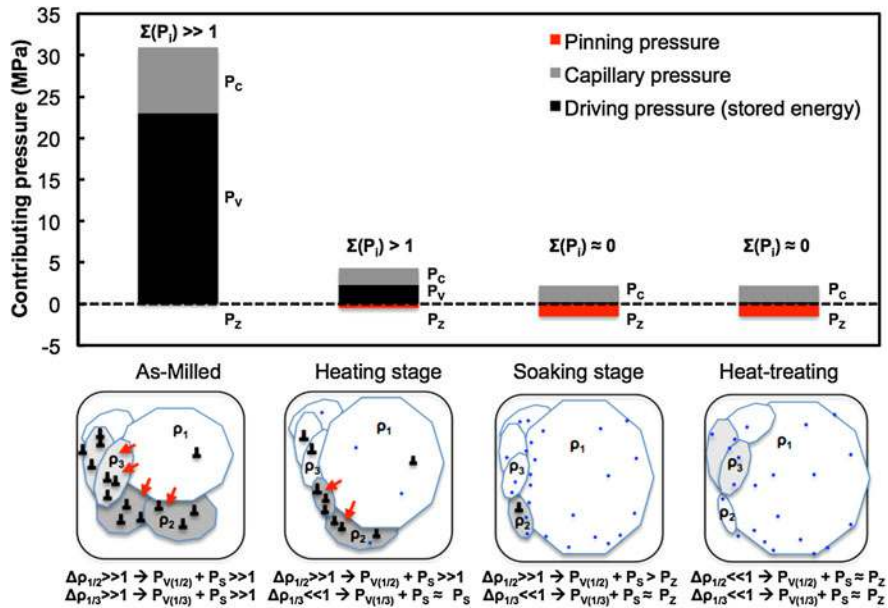


Fig. 8—Evolution of the contributing mechanisms to grain growth along the processing route. Pressures are calculated according to the measured microstructural features, as recalled in Table II. Pinning pressure is taken negative due to its competition with the driving pressures. Interactions between grains (1/2 and 2/3) are described along the process. Nano-oxides are represented by blue dots (Color figure online).

sure for grain growth.<sup>[29]</sup> This kind of data is difficult to obtain in mechanically alloyed industrial steels where driving pressure is unlikely a constant.

## VI. CONCLUSIONS

A mechanically alloyed ferritic ODS steel was consolidated by SPS and HIP. A multiscale characterization was performed after consolidation and subsequent heat-treating, providing substantial insight on the grain growth mechanisms.

1. The resulting grain structure was observed to be heterogeneous with both ultra-fine grains and much larger grains. Appearance of this structure was explained by the initial heterogeneous spatial distribution of stored energy due to high-energy attrition of the MA powder, which induced inhomogeneous recrystallization of the grains. The local driving pressure is so high that new nuclei rapidly grow at the expense of the deformed ones. Until recovery has been completed, recrystallized grains are highly mobile even if precipitation has started. Thus, plastic work due to milling is the cause of the so-called abnormal growth. Consequently, this scenario could be applied to any metallic materials that have been deformed in a heterogeneous manner, particularly by high-energy milling.
2. Only completed recovery and precipitation are able to impede grain growth. Once the stored energy has been lowered, the dense dispersion of nanoparticles is effective to pin grain boundaries. The strong resistance to coarsening of the nano-oxides formed during consolidation justifies the extreme thermal stability of the ultra-fine grains. Calculations of critical grain size due to pinning effect from Zener and Rios give rise to a range of grain mean radii between 40 and 270 nm, respectively (Table II). This corresponds to the size range of remaining ultra-fine grains.
3. Precipitation is not the major cause of abnormal growth but is responsible for thermal stability of heterogeneous fine structure. This highlights the importance of precipitation that not only brings effective Orowan strengthening but also is a key-factor for the stability of the UFG that enhances Hall–Petch hardening.

Further work will be focusing on *in situ* studies of microstructural instabilities of such milled powder to quantify the kinetics of recovery and recrystallization with respect to precipitation in order to be able to manage the grain structure during consolidation.

## ACKNOWLEDGMENTS

The authors express their gratitude to F. Mercier and G. Bonnefont for the excellent technical assistance

for SPS consolidation and to D. Hamon and S. Urvoy for their contribution in materials characterization. Thanks are also due to the CLYM (Centre Lyonnais de Microscopie) for the access to the FIB/SEM device used in this study. This work was partly supported by the European community within the FP7 Project MATTER and performed with financial support for the French CNRS GdR GEDEPEON. This study was made in the frame of a tripartite agreement between the CEA, AREVA NP, and EDF.

## REFERENCES

1. S. Ukai, M. Harada, H. Okada, M. Inoue, S. Nomura, S. Shikakura, T. Nishida, M. Fujiwara, and K. Asabe: *J. Nucl. Mater.*, 1993, vol. 204, pp. 65–73.
2. R.L. Klueh, D.S. Gelles, S. Jitsukawa, A. Kimura, G.R. Odette, B. van der Schaaf, and M. Victoria: *J. Nucl. Mater.*, 2002, vols. 307–311, pp. 455–65.
3. P. Dubuisson, Y. de Carlan, V. Garat, and M. Blat: *J. Nucl. Mater.*, 2012, vol. 428, pp. 6–12.
4. M.J. Alinger, G.R. Odette, and D.T. Hoelzer: *Acta Mater.*, 2009, vol. 57, pp. 392–406.
5. I. Lonardelli, M. Bortolotti, W. Van Beek, L. Girardini, M. Zadra, and H.K.D.H. Bhadeshia: *Mater. Sci. Eng. A*, 2012, vol. 555, pp. 139–47.
6. G. Ji, T. Grosdidier, N. Bozzolo, and S. Launois: *Intermetallics*, 2007, vol. 15, pp. 108–18.
7. D. Fabrègue, J. Piallat, E. Maire, Y. Jorand, V. Massardier-Jourdan, and G. Bonnefont: *Powder Metall.*, 2012, vol. 55, pp. 76–79.
8. R. Orru, R. Licheri, M. Locci, A. Cincotti, and G. Cao: *Mater. Sci. Eng. R*, 2009, vol. 63, pp. 127–287.
9. X. Boulnat, D. Fabrègue, M. Perez, M.H. Mathon, and Y. de Carlan: *Metall. Mater. Trans. A*, 2013, vol. 44A, pp. 2461–65.
10. C. Menapace, I. Lonardelli, M. Tait, and A. Molinari: *Mater. Sci. Eng. A*, 2009, vol. 517, pp. 1–7.
11. Y. Wang, M. Chen, F. Zhou, and E. Ma: *Nature*, 2002, vol. 419, p. 912.
12. C.C. Koch: *Scripta Mater.*, 2003, vol. 49, pp. 657–62.
13. A. Mukherjee: *Mater. Sci. Eng. A*, 2002, vol. 322, pp. 1–22.
14. B. Srinivasarao, K. Oh-ishi, T. Ohkubo, and K. Hono: *Acta Mater.*, 2009, vol. 57, pp. 3277–86.
15. Cs. Balázi, F. Gillemot, M. Horváth, F. Wéber, K. Balázi, F. Cinar Sahin, Y. Onüralp, and A. Horváth: *J. Mater. Sci.*, 2011, vol. 46, pp. 4598–605.
16. M. Cabibbo, C. Paternoster, R. Cecchini, A. Fabrizi, A. Molinari, S. Libardi, and M. Zadra: *Mater. Sci. Eng. A*, 2008, vol. 496, pp. 121–32.
17. W.J. Kim, I.K. Moon, and S.H. Han: *Mater. Sci. Eng. A*, 2012, vol. 538, pp. 374–85.
18. M. Ferry and F.J. Humphreys: *Acta Mater.*, 1996, vol. 44 (4), pp. 1293–1308.
19. J. Humphreys: *Acta Mater.*, 1997, vol. 45 (12), pp. 5031–39.
20. H. Jazaeri and F.J. Humphreys: *Acta Mater.*, 2004, vol. 52, pp. 3251–62.
21. E. Nes: *Scripta Metall.*, 1976, vol. 10, pp. 1025–28.
22. S.Y. Zhong, J. Ribis, V. Klosek, Y. de Carlan, N. Lochet, V. Ji, and M.H. Mathon: *J. Nucl. Mater.*, 2012, vol. 428, pp. 154–59.
23. C.A. Williams, P. Unifantowicz, N. Baluc, G.D.W. Smith, and E.A. Marquis: *Acta Mater.*, 2013, vol. 61, pp. 2219–35.
24. Y. Liu, J. Zhoua, and X. Linga: *Mater. Sci. Eng. A*, 2010, vol. 527, pp. 1719–29.
25. Z. Dapeng, L. Yong, L. Feng, W. Yuren, Z. Liujie, and D. Yuhai: *Mater. Lett.*, 2011, vol. 65, pp. 1672–74.
26. C. Heintze, M. Hernández-Mayoral, A. Ulbricht, F. Bergner, A. Shariq, T. Weissgärber, and H. Frielinghaus: *J. Nucl. Mater.*, 2012, vol. 428, pp. 139–46.
27. M.H. Mathon, M. Perrut, S.Y. Zhong, and Y. de Carlan: *J. Nucl. Mater.*, 2012, vol. 428, pp. 147–53.
28. J. Ribis and Y. de Carlan: *Acta Mater.*, 2012, vol. 60, pp. 238–52.

29. F.J. Humphreys and M. Hatherly: *Recrystallization and Related Annealing Phenomena*, 2nd ed., Elsevier, Amsterdam, 2004.
30. A. Michels, C.E. Krill, H. Ehrhardt, R. Birringer, and D.T. Whu: *Acta Mater.*, 1999, vol. 47 (7), pp. 2143–52.
31. D.G. Cram, X.Y. Fang, H.S. Zurob, Y.J.M. Bréchet, and C.R. Hutchinson: *Acta Mater.*, 2012, vol. 60, pp. 6390–6404.
32. T. Gladman: *Proc. R. Soc. Lond. A*, 1966, vol. 294A, p. 298.
33. C. Zener, quoted by C.S. Smith, *Trans. Met. Soc. AIME*, 1948, vol. 175, pp. 15–51.
34. P.R. Rios: *Acta Metall.*, 1987, vol. 35, p. 28025.
35. F. Haessner and J. Schmidt: *Scripta Metall.*, 1988, vol. 22, pp. 1917–22.
36. E. Schmidt, P. Nagpal, and I. Baker: *Mater. Res. Soc. Proc.*, 1989, vol. 133, pp. 755–60.
37. M. Calcagnotto, D. Ponge, E. Demir, and D. Raabe: *Mater. Sci. Eng. A*, 2010, vol. 527, pp. 2738–46.
38. X.C.H. Wu, S. Ukai, R. Miyata, N. Oono, S. Hayashi, B. Leng, S. Ohtsuka, and T. Kaito: *J. Nucl. Mater.*, 2013, vol. 440, pp. 553–56.
39. L.P. Kubin and A. Mortensen: *Scripta Mater.*, 2003, vol. 48, pp. 119–25.
40. H. Gao, Y. Huang, W.D. Nix, and J.W. Hutchinson: *J. Mech. Phys. Solids*, 1999, vol. 47, pp. 1239–63.
41. A. Molinari, S. Libardi, M. Leoni, and P. Scardi: *Acta Mater.*, 2010, vol. 58, pp. 963–66.
42. H. Sakasegawa, L. Chaffron, F. Legendre, L. Boulanger, T. Cozzika, M. Brocq, and Y. de Carlan: *J. Nucl. Mater.*, 2009, vol. 384, pp. 115–18.
43. V. de Castro, E.A. Marquis, S. Lozano-Perez, R. Pareja, and M.L. Jenkins: *Acta Mater.*, 2001, vol. 59, pp. 3927–36.
44. M. Ratti, D. Leuvrey, M.H. Mathon, and Y. de Carlan: *J. Nucl. Mater.*, 2009, vols. 386–388, pp. 540–43.
45. C. Cayron, A. Montani, D. Venet, and Y. de Carlan: *J. Nucl. Mater.*, 2010, vol. 399, p. 219.
46. M. Klimiankou, R. Lindau, and A. Möslang: *J. Nucl. Mater.*, 2004, vols. 329–333, pp. 247–51.
47. Y. Wu, E.M. Haney, N.J. Cunningham, and G.R. Odette: *Acta Mater.*, 2012, vol. 60, pp. 3456–68.
48. H. Kishimoto, R. Kasada, O. Hashitomi, and A. Kimura: *J. Nucl. Mater.*, 2009, vol. 386, p. 533.
49. H.K.D.H. Badeshia: *Mater. Sci. Eng. A*, 1997, vol. 223, pp. 64–77.
50. M. Perez and A. Deschamps: *Mater. Sci. Eng. A*, 2003, vol. A360, pp. 214–19.
51. F. Perrard, A. Deschamps, and P. Maugis: *Acta Mater.*, 2007, vol. 55, pp. 1255–66.
52. R. Wagner and R. Kampmann: in *Phase Transformations in Materials*, G. Kostorz, ed., Wiley, Weinheim, 2001.
53. Y. Huang, F.J. Humphreys, and M. Ferry: *Acta Mater.*, 2000, vol. 48, pp. 2543–56.
54. A. Hirata, T. Fujita, Y.R. Wen, J.H. Schneibel, C.T. Liu, and M.W. Chen: *Nature Mater.*, 2011, vol. 10, pp. 922–26.